

Article

Research and Evaluation of Foam-Drainage Corrosion-Inhibition Hydrate Anti-Aggregation Integrated Agent

Weijun Ni ¹, Guohao Yang ¹, Jie Dong ^{2,3,*}, Yansong Pan ², Gang Chen ²  and Xuefan Gu ^{4,*}

¹ College of Petroleum Engineering, Xi'an Shiyou University, Xi'an 710065, China; wjni@xsyu.edu.cn (W.N.); 21211010004@stumail.xsyu.edu.cn (G.Y.)

² Shaanxi University Engineering Research Center of Oil and Gas Field Chemistry, Xi'an Shiyou University, Xi'an 710065, China; 22212071107@stumail.xsyu.edu.cn (Y.P.); gangchen@xsyu.edu.cn (G.C.)

³ Sinopec Shanghai Gaoqiao Petrochemical Co., Ltd., Shanghai 200129, China

⁴ Shaanxi Province Key Laboratory of Environmental Pollution Control and Reservoir Protection Technology of Oilfields, Xi'an Shiyou University, Xi'an 710065, China

* Correspondence: 20212070841@stumail.xsyu.edu.cn (J.D.); xuefangu@xsyu.edu.cn (X.G.)

Abstract: In natural gas exploitation, foam drainage, corrosion inhibition and hydrate inhibition of wellbore fluid are conventional operations. However, there is often a problem where multiple chemical agents cannot be effectively used together and can only be used separately, resulting in complex production processes. In this study, the final integrated formulation was determined: 0.1% sodium alpha-olefin sulfonate (AOST) + 0.3% dodecyl dimethyl betaine (BS-12) + 0.3% sodium lignosulfonate + 0.5% hydrazine hydrate. The minimum tension of the integrated agent could be reduced to 23.5 mN/m. The initial foaming height of the integrated agent was 21.5 cm at 65 °C, the liquid-carrying capacity was 143 mL, and the liquid-carrying rate reached 71.5%. The maximum corrosion depth also decreased from 11.52 μm without the addition of hydrazine hydrate, gradually decreasing to 5.24 μm as the concentration of hydrazine hydrate increased. After adding an integrated agent, the growth rate of hydrates was slow and aggregation did not easily occur, and the formation temperature was also more demanding. Therefore, the integrated agent has an inhibitory effect on the formation of hydrates and has a good anti-aggregation effect. From the observation of the microstructure, the emulsion is an oil-in-water type, and the integrated agent adsorbs at the oil–water interface, preventing the dispersed water droplets in the oil phase from coalescing in one place. The oil-in-water type emulsion is more likely to improve the performance of the natural gas hydrate anti-aggregation agent.

Keywords: foaming agent; foaming stability; surface tension; microstructure; salt resistance



Citation: Ni, W.; Yang, G.; Dong, J.; Pan, Y.; Chen, G.; Gu, X. Research and Evaluation of Foam-Drainage Corrosion-Inhibition Hydrate Anti-Aggregation Integrated Agent. *Processes* **2023**, *11*, 2745. <https://doi.org/10.3390/pr11092745>

Academic Editors: Aijun Guo, Dicho Stratiev and Dobromir Yordanov

Received: 6 August 2023

Revised: 30 August 2023

Accepted: 10 September 2023

Published: 14 September 2023



Copyright: © 2023 by the authors. Licensee MDPI, Basel, Switzerland. This article is an open access article distributed under the terms and conditions of the Creative Commons Attribution (CC BY) license (<https://creativecommons.org/licenses/by/4.0/>).

1. Introduction

As an effective method to solve bottom-hole fluid accumulation, foam-drainage agents have become an economically efficient and commonly used auxiliary recovery method, and most studies have verified their economic and effective characteristics. In order to develop a high-performance foam-dispersant system, different types of surfactants were compounded [1–9]. In the process of natural gas development, there is not only the problem of liquid accumulation, but also the problem of hydrate and pipeline corrosion in an environment of low temperature and high pressure. For research into an integrated agent that has the simultaneous functions of foam drainage, corrosion inhibition and hydrate anti-polymerization, the combination of any two commonly used agents may produce antagonism [10–17]. For example, methanol is often added for the purpose of hydrate anti-polymerization to alleviate the accumulation of hydrate, and methanol has an obvious effect as an anti-polymerization agent, However, methanol plays a defoaming role in foam

dispersants, while commonly used corrosion inhibitors lack the performance of hydrate anti-aggregation.

Cage hydrates are ice-like compounds composed of small gas molecules encapsulated in water molecules. The formation of natural gas hydrates in oil and gas pipelines may lead to the failure of natural gas flow and serious safety and environmental issues. The use of anti-condensates is a promising method to reduce the risks of natural gas hydrates in actual production [18]. Therefore, effectively suppressing the generation and blockage of hydrates is a very important and urgent problem for all oil and gas production. One of the most effective methods to improve natural gas extraction is to suppress the generation of natural gas hydrates. Due to the fact that the use of anti-polymerization agents is not limited by temperature (supercooling) conditions and the concentration of use is below 3%, the price of anti-polymerization agents is relatively high [19]. Considering the economic benefits, in practical production applications, different types of inhibitors are often mixed and reused to reduce costs. This can significantly improve both economic composition and the inhibition effect. At present, this method is the most widely used in the development and application of natural gas in domestic and foreign gas fields to suppress hydrate generation and accumulation [20,21].

To address the issues of high water content in gas wells, hydrate formation under low temperature and high pressure, and wellbore-corrosion susceptibility, a foam-drainage hydrate anti-aggregation corrosion-inhibitor system has been developed. By utilizing experimental and theoretical research, we evaluated the foaming and stabilizing properties of the foam-drainage hydrate anti-aggregation corrosion-inhibitor system, and revealed the relationship between the structure of the foaming agent and the foaming performance [22–26]. We tested the phase-change point of hydrate formation caused by the system, and explored the corrosion-inhibition performance of the system for injection and production systems such as wellbore [27–30]. Therefore, based on these three points, a foam-agent system with the multiple performances of foaming, polymerization prevention and corrosion inhibition has been developed.

2. Experimental

2.1. Materials

AOST was purchased from Lusen Chemical Co., Ltd. (Linyi, China). BS-12 was purchased from Huajun New Materials Co., Ltd. (Huainan, China). Methanol and petroleum ether were purchased from Fuyu Fine Chemical Co., Ltd. (Tianjin, China). All products were used as received without further purification.

2.2. Surface-Tension Measurement

The surface tension of each solution was measured by the hanging-ring method at room temperature. Before the measurements, the tensiometer (Kruss K 100, Hamburg, Germany) was used to test the surface tension of a distilled water sample to confirm the accuracy of the instrument; the surface tension of distilled water measured in this manner was 72.65 mN/m. Each measurement was repeated at least three times and results reported as the average.

2.3. Foaming-Capacity Evaluation

A high-speed agitation method was used to generate foams using a high-speed mixer (GJ-3S, Qingdao Haitongda Special Instrument Co., Ltd., Qingdao, China). In each test, 100 mL surfactant solution was agitated at 7000 r/min for 3 min at ambient conditions. After the foam preparation, the foam was transferred into a graduated cylinder immediately. The volume and half-life time (the time that 50 mL of free-water phase accumulated at the bottom of the cylinder) of the foam were recorded. Each test was repeated in triplicate. All measurements were performed at 25 °C and atmospheric pressure.

2.4. Salt-Resistance Evaluation

Generally, the salinity of formation water has a strong adverse effect on the generation of foam. To study the effect of concentration and species of inorganic ions on the foaming ability and related foaming stability of the surfactants, surfactant solutions with different salt concentrations (NaCl, KCl, MgCl₂, CaCl₂) were prepared.

2.5. Temperature Resistance

The temperature in a well has a significant effect on the performance of foaming agents. Therefore, the Ross–Miles method was used to measure the foaming capacity and stability of the formula at temperatures ranging from 30 to 70 °C. Each test was repeated three times.

2.6. Methanol Effect Evaluation

During gas production, methanol was usually used to prevent the formation of gas hydrate. However, the presence of methanol may also retard the performance of foaming agents. Therefore, it was necessary to check the methanol's influence on the foaming ability of the optimized foaming agents. In this section, the foaming performance of optimized surfactant solutions with 0, 5, 10 and 15% methanol was tested in a temperature range of 40 to 70 °C using the Ross–Miles method.

2.7. Liquid-Carrying-Capacity Test

According to the performance requirements for the foam-discharge agent in the Changqing Gas Field, the liquid-carrying performance of the integrated agent required evaluation. After aging 200 mL of the integrated agent at 65 °C for 30 min, 3.0 L/min of N₂ was introduced into the dedicated foam tube. After 15 min, the volume vs. of the remaining liquid in the foam tube was recorded. The formula for calculating the liquid-carrying rate is:

$$W = \frac{200 - V_s}{200} \times 100\%$$

where W is liquid-carrying rate (%), V_s is the remaining liquid in the foam tube.

2.8. Adsorption Experiment

By scanning the wavelength of a UV spectrophotometer, the adsorption capacity of different concentrations of 4DF-4 as a whole agent on iron powder was tested, and the adsorption relationship between 4DF-4 as a foaming agent and metals was evaluated using a standard curve.

2.9. Surface Micromorphology of Steel Sheet

A DSX-500 (OLYMPUS, Tokyo, Japan) fully automatic three-dimensional imaging microscope was used to scan steel sheets in bright field (BF) mode, the scanning area of the Q235 sample was 277 μm × 277 μm, in order to obtain 2D and 3D images as well as height maps.

2.10. Micro-Morphology of Hydrates

The assembled hydrate-growth observation instrument, consisting of temperature control system, low-temperature reaction system, and image processing system, was used to observe the micro-morphology of hydrate growth of 20% tetrahydrofuran aqueous solution and 20% tetrahydrofuran integrated agent solution at different times.

2.11. Contact-Angle Experiment

The contact angle of water and oil droplets on the surface of glass treated with reagents was measured using a contact-angle measuring instrument.

2.12. Thermodynamic Analysis of Hydrates

The phase-transition point of hydrate with 20% tetrahydrofuran aqueous solution and 20% tetrahydrofuran surfactant solution was measured by DSC.

2.13. Emulsification Experiment and Microstructure Analysis after Emulsification

Samples of 10 mL of different concentration multiples (times 0.5, 1, 1.5, 2) were taken of the integrated agent and condensate oil in a 1:1 ratio and placed in a centrifuge tube. They were placed in a 45 °C water bath at a constant temperature for 10 min and then taken out. They were shaken in the left and right hands 50 times each to form an emulsion, then placed in a water bath and the time and amount of water released was recorded. The precipitation rate was calculated:

$$V_w = \frac{V_T}{V_0} 100\%$$

where V_w is precipitation rate (%), V_T is the volume of water that separates water (mL), V_0 is the total volume of water (mL).

Samples of 100 mL of different concentration multiples (times 0.5, 1, 1.5, 2) were taken of the integrated agent and crude oil in a 1:1 ratio and placed in a high stirring cup. After stirring according to the high-stirring evaluation method, the emulsion was placed under a polarizing microscope to observe the micro-morphology of the emulsion of the integrated agent and oil at different concentrations.

3. Results and Discussion

3.1. Measurement of Surface Tension

From Tables 1 and 2, it can be seen that the interfacial tension value gradually decreased with the increase in the concentration of the integrated agent, and the tension changed more rapidly in the low-concentration range. This is mainly because the surface molecules of the solution are oriented and continuously form a single molecular layer of the integrated agent. The hydrophobic end arrangement increased, and the surface tension decreased until the critical micelle concentration was reached. At this point, the surface tension appeared to have a turning point, and the surface tension value was 23.5 mN/m. Due to the lack of interfacial activity in the micelles inside the solution, the interfacial tension tends to stabilize. As the concentration increased, there was a slight increase in surface tension, which may be due to the diversification of the integrated agent and the formation of complex micelles, thereby affecting the molecular concentration on the surface and causing changes in surface and interfacial tension [31,32]. The same applies to the variation of interfacial tension, with a minimum value of 2.3×10^{-2} mN/m.

Table 1. Surface tension values of the integrated agent at different concentrations.

Concentration/%	0.00001	0.0001	0.001	0.005	0.01	0.05	0.1	0.5	0.8	1.2
Tension value/mN/m	32.6	31.3	30.1	26.1	25.4	23.5	23.9	24.7	24.3	24.8

Table 2. The interfacial tension value of the one-piece agent at different concentrations (60 °C).

Concentration/%	0.024	0.06	0.12	0.24	0.6	1.2
Tension value/mN/m	2.12	1.244	7.1×10^{-1}	2.3×10^{-2}	1.2×10^{-1}	1.5×10^{-1}

3.2. Mineral-Content Impact Test

From Table 3, it was found that after the addition of salt, the four types of salts had an adverse effect on the foaming ability of the integrated agent. The negative effect of salt on the foaming ability of the integrated agent may be attributed to the obstruction of electrostatic repulsion between charged bubble surfaces, thereby reducing the foaming ability. However, relatively speaking, the salt resistance of the all-in-one agent was ranked as follows: KCl > NaCl > MgCl₂ > CaCl₂.

Table 3. Foaming performance of the integrated agent under different salt concentrations.

Concentration of NaCl/%	Initial Height of the Foam/cm	Concentration of KCl/%	Initial Height of the Foam/cm	Concentration of CaCl ₂ /%	Initial Height of the Foam/cm	Concentration of MgCl ₂ /%	Initial Height of the Foam/cm
0	21.3	0	21.3	0	21.3	0	21.3
2.5	16.7	2.5	17.8	2.5	8.3	2.5	14.8
5	15.6	5	18.0	5	5.9	5	10.1
10	12.3	10	17.5	10	4.2	10	6.6
20	3.9	20	8.7	20	2.5	20	3.2

3.3. Temperature-Resistance Evaluation

It can be seen from Table 4 that the initial foam height increased with the increasing temperature, but the higher the temperature, the faster the defoaming speed of the foam, and the stability decreased. When the temperature was raised, the activity of the integrated agent molecules was enhanced, and foam was more likely to be generated. When the test temperature was low (30, 40 °C), the height of the foam almost did not change with the extension of time. This is because when the temperature is low, the water loss rate of the liquid film is slow, and the gas movement is slow, resulting in the low diffusion ability of the gas in the small bubbles to the large bubbles, so that the foam has better stability. The higher temperature (50~70 °C) will make the water molecules more likely to evaporate, the loss rate of liquid on the liquid film will be accelerated, and the thickness of the liquid film will continue to decrease due to the loss of liquid, so the foam is more likely to break, leading to the decrease in the height of the foam. In addition, high temperature will also accelerate the diffusion of gas in the foam and accelerate the diffusion of gas in small bubbles to large bubbles, thus shortening the life of the foam.

Table 4. Foaming properties of the one-piece agent at different temperatures.

Temperature/°C	0 min/cm	5 min/cm	10 min/cm	15 min/cm	20 min/cm
30	21.3	21.7	21.7	21.3	21.0
40	21.5	22.0	21.9	20.5	20.3
50	21.9	22.3	20.0	13.8	7.9
60	22.3	22.9	12.5	7.8	5.4
70	22.6	23.6	7.3	3.9	3.0

3.4. Methanol-Resistance Test

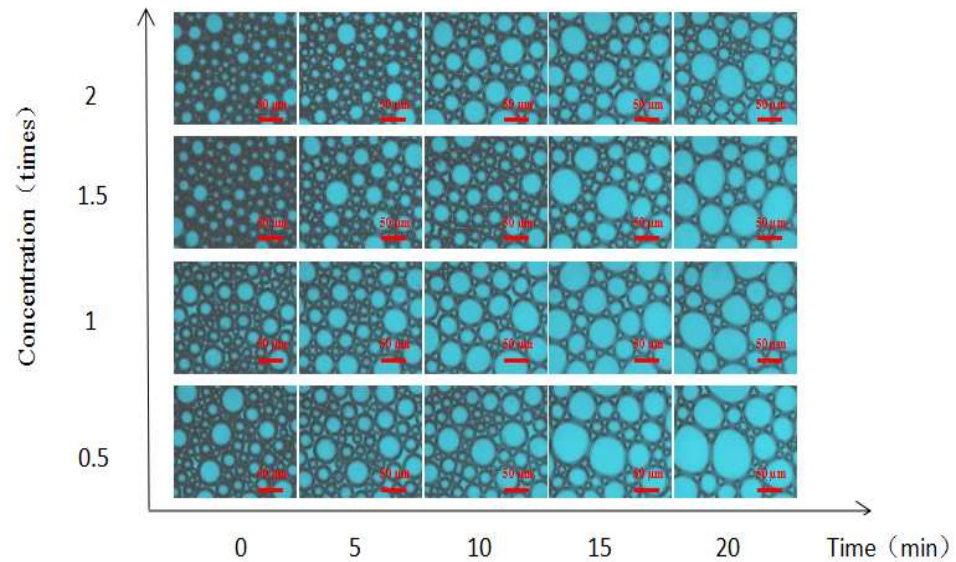
Different concentrations of methanol were added to verify the impact of methanol on the integrated agent, ensuring that the existing methanol in the formation interfered with the foam removal performance of the integrated agent when used as an anti-aggregation agent. It can be seen from Table 5 that the initial height of the foam decreased from 18.5 to 14.0 cm when the concentration of methanol continued to increase. With the extension of time, the height of the foam changed little, and the height of the foam decreased slightly. This is because methanol molecules are easily spread on the surface of liquid film, and they do not have amphiphilic properties. They grab the arrangement position of the integral agent molecules on the surface of the liquid film, leading to the inability of the ordered and directional arrangement of the monolayers in the interface. It has a defoaming effect. The experiment shows that methanol does have an impact on the foaming performance of the integrated agent, but the impact is not significant.

Table 5. Foaming performance of the one-piece agent under different methanol concentrations.

Concentration/%	0 min/cm	5 min/cm	10 min/cm	15 min/cm	20 min/cm
5	18.5	18.5	18.0	18.0	17.9
10	17.0	17.0	16.9	16.9	16.7
20	14.0	13.9	13.8	13.5	13.3
30	14.0	13.5	13.3	13.2	12.9

3.5. Analysis of Foam Microstructure

It can be seen from Figure 1 that the microstructure of foam with different concentrations of integrated agent is similar under the polarizing microscope, but over the same time, with the increase in concentration, the numbers of small foam increased significantly, the liquid film thickness was thicker, and the liquid loss rate slowed down. At a certain concentration, with the increase in time, the liquid on the foam liquid film was gradually lost and the gas wrapped by the foam continuously diffused, the volume of foam gradually increased, the thickness of the liquid film decreased, and small bubbles continued to bubble into the atmosphere until the foam burst. It can be seen from the figure that at 20 min, no matter whether the concentration of the integrated agent was 0.5, 1, 1.5 times or twice the standard concentration, the foam morphology had no obvious polygon structure, which means that the integrated agent molecules were arranged in an orderly fashion on the liquid film to maintain the water content of the liquid film, reduce its flow loss and gas diffusion, and finally maintain the stability of the foam. In addition, the foam took a long time to be broken, which can also prevent it from falling back in the process of carrying liquid accumulation upward, so the microscopic view of foam can well demonstrate the performance of the foam discharge capacity of the integrated agent.

**Figure 1.** The microstructure of the integrated agent at different times.

3.6. Liquid-Carrying Capacity

In practical applications, the foam removal agent needs to carry the accumulated liquid from the bottom of the well out of the formation, so it was necessary to simulate the actual operation with the assistance of a certain airflow to achieve the corresponding liquid-carrying capacity. The magnitude of the liquid-carrying rate also represents the strength of the foam-removal capacity. Moreover, in actual production, the foam-removal agent also needs to overcome the influence of temperature. Therefore, the experimental temperature was set at 65 °C, and a certain flow rate of N₂ was introduced to record the liquid-carrying capacity, which was compared with the representative company's liquid-carrying-capacity

standard, The experimental results are shown in the following table. It can be seen from Table 6 that the initial foaming height of the integrated agent measured at 65 °C was 215 mL, and the foaming height after 5 min was 245 mL, because high temperature will enhance the activity of surfactant molecules, so the foam height will increase in a short time. The liquid-carrying capacity of the integrated agent was 143 mL, with a liquid-carrying rate of 71.5%, which is much higher than the requirements of the Changqing Gas Field for the liquid-carrying capacity of the foam-discharge agent. Therefore, this integrated agent has certain on-site application value.

Table 6. Foaming ability and liquid-carrying ability of one-piece agent (65 °C).

Content	Changqing Gas Field (Yulin)/mL	Changqing Gas Field (Shenmu)/mL	One-Piece Agent/mL
Foam height (0 min)	120	110	215
Foam height (5 min)	70	60	245
Liquid-carrying capacity (0~15 min)	120	110	143

3.7. Viscoelasticity of Foam

As shown in Figure 2, within a certain concentration range of $1 \times 10^{-7} \sim 1 \times 10^{-5}$ g/mL, the intermolecular force increased and the interfacial activity increased, resulting in an increase in the interfacial expansion modulus and viscoelasticity. As the concentration of the integrated agent ($1 \times 10^{-4} \sim 1 \times 10^{-2}$ g/mL) continued to increase, the interfacial expansion modulus and viscoelasticity decreased. The high concentration of the integrated agent will lead to an accelerated diffusion exchange between the interface and the bulk phase, resulting in the reduction in the interfacial expansion modulus [33], and the foam tends to be stable. Not only the concentration increased; there were maximum values for the expansion modulus, elastic and viscous modulus, and phase angle, which were 32.32 mN/m, 29.86 mN/m, 483.33 mN/m, and 31.96° , respectively.

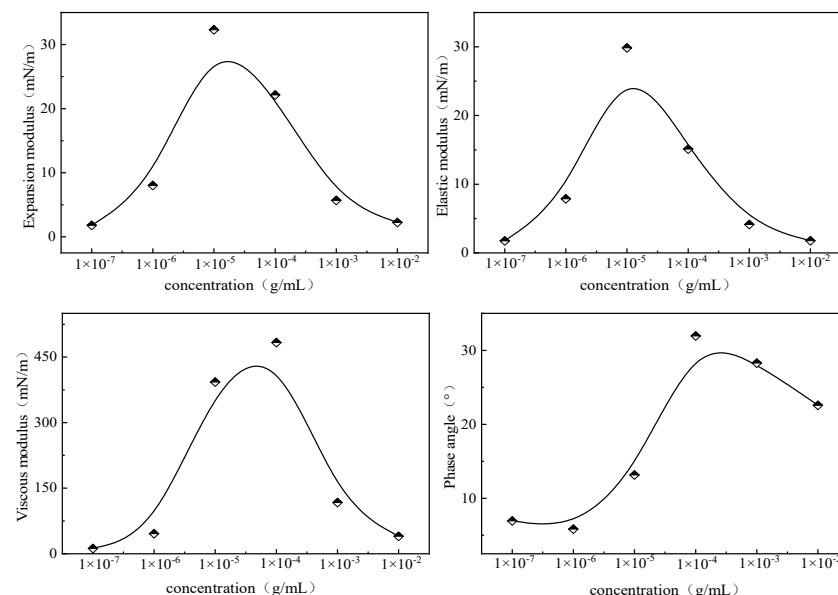


Figure 2. Interfacial viscoelasticity measurements at different concentrations.

3.8. Adsorption Experiment

Figure 3 of the adsorption experiment shows the UV spectra of the integrated agent with different concentration multiples. The absorption peak generated at 362 nm showed a significant red shift with the increase in concentration and Fe powder, and the absorption peaks were all enhanced. This may be due to the integrated agent adsorbing on the surface

of Fe atoms and coordinating with metal ions. This indicates that the integrated agent molecules adsorb on the surface of carbon steel, forming a tight and stable adsorption film that can effectively prevent the occurrence of steel plate corrosion.

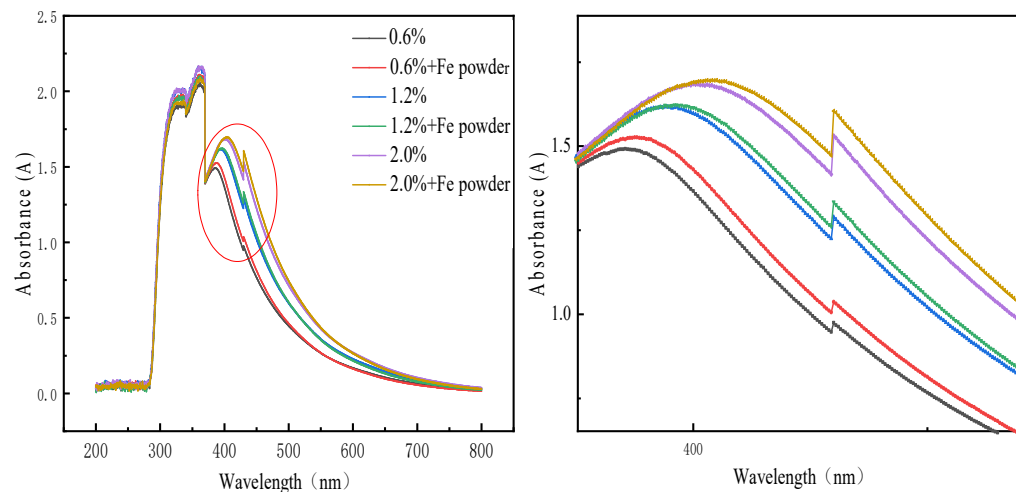


Figure 3. Wavelength scanning of the one-piece agent at different concentrations.

3.9. Surface Micromorphology of Metal

A model of the steel sheet surface and pitting pits shown on the right of Figure 4 was established, and the morphology of the steel sheet was indirectly observed. From the 2D images in Figure 4, it can be observed that the surface of the steel sheet was smooth, and the 4DF system had a significant promoting effect on the corrosion inhibition of the steel sheet. As the concentration of hydrazine hydrate increased, the surface roughness decreased and the corrosion degree of the steel sheet significantly decreased. Compared with the blank group (without any additives), the 4DF system showed a significant reduction in pitting pits. The more purple in the 3D and height maps, the deeper the pitting pits. Figure 4 showed that the purple area significantly decreased and the pitting range significantly decreased, following the increase in hydrazine hydrate concentration. The maximum corrosion depth decreased to 5.24 μm , proving that the 4DF system can effectively suppress the corrosion of steel sheets and play a good corrosion-inhibition role.

3.10. Microscopic Morphology of Hydrate Growth

Due to the difficulty in forming hydrates in normal environments, the formation of tetrahydrofuran hydrates using self-built instruments was studied and discussed. Figure 5 shows the growth morphology of the hydrates as time increased at 2 $^{\circ}\text{C}$. It can be seen that from 0 s onwards, hydrates continued to form at the edge of the liquid surface and attracted each other towards the middle of the droplets. This is because there is a cohesive force between the formed hydrate and the forming hydrate, which forces them to attract and aggregate with each other. Moreover, there is a certain repulsive effect at the interface between the formed hydrate and the formed hydrate, causing the formed hydrate to continuously aggregate towards the middle.

As shown in Figure 6, At -1°C , the structure of the THF hydrate was more loose and the hydrate formation rate slowed down compared to the THF hydrate added as a whole agent. At 30 s, the 20% THF hydrate was basically completely formed and mostly generated giant crystals, while the hydrate containing an organic agent was only generated on a large scale at 60 s. At 0 $^{\circ}\text{C}$ for 60 s, the hydrate crystal structure formed by 20% THF was significantly more compact. At 1 $^{\circ}\text{C}$, the risk of hydrate formation was significantly reduced after the addition of an integrated agent, which grew slowly and was looser compared to the hydrates formed without an integrated agent. It did not aggregate into large-scale crystals due to the arrangement and adsorption of integrated agent molecules on the surface of the hydrates. The

charge of hydrophilic groups in the integrated agent can repel each other, thereby preventing the aggregation of hydrates [28]. In summary, the integrated agent has an inhibitory effect on the formation of THF hydrates and has a good anti-aggregation effect.

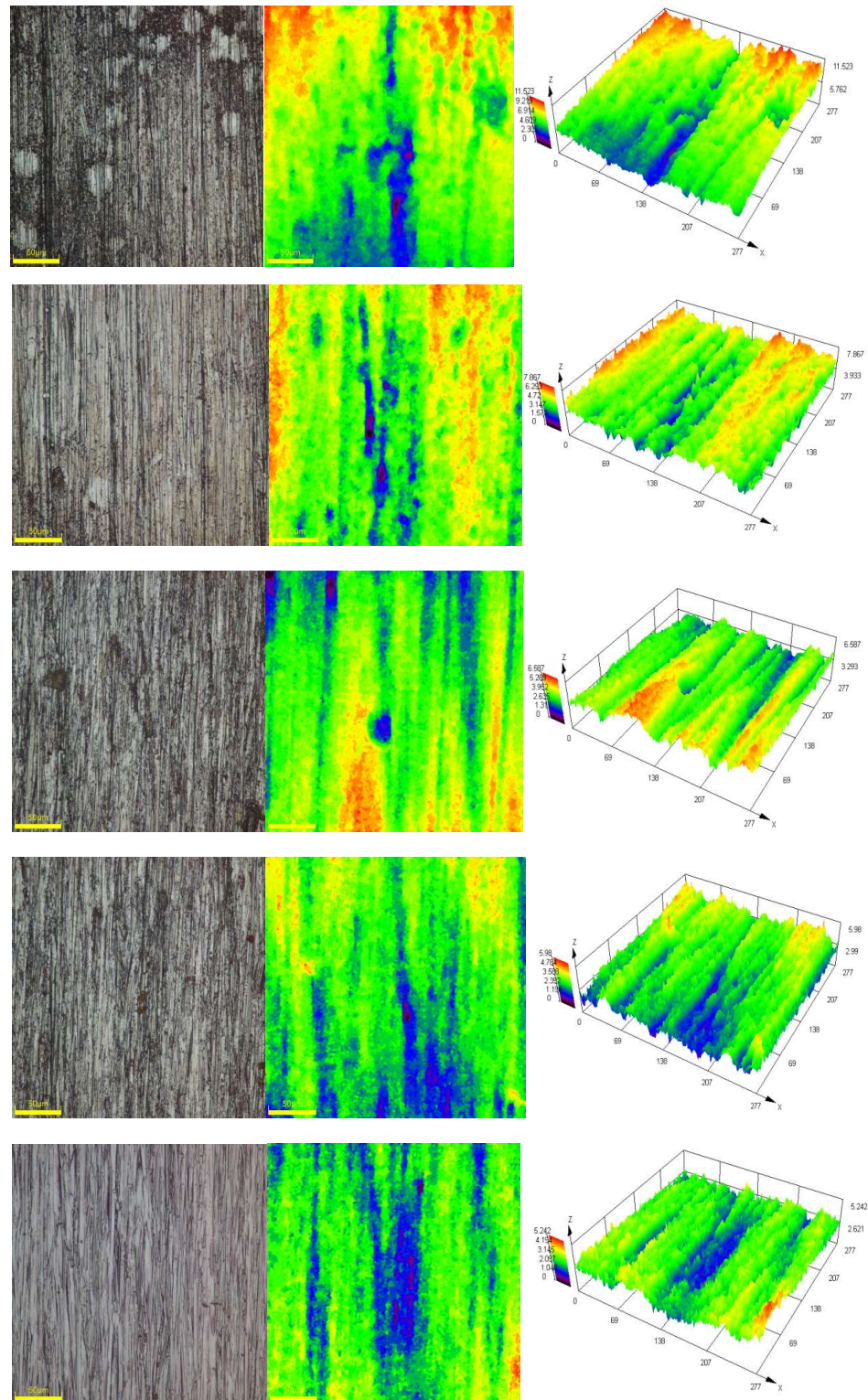


Figure 4. Two-dimensional view, height map and three dimensional view (1000 magnification) of the steel sheet under different concentrations of hydrazine hydrate in the all-in-one agent.

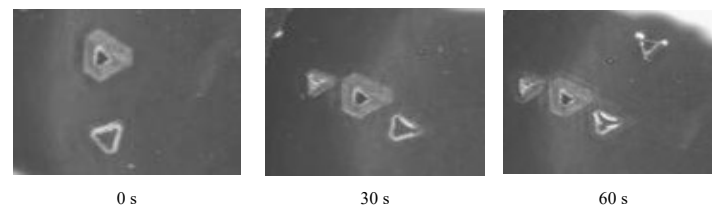
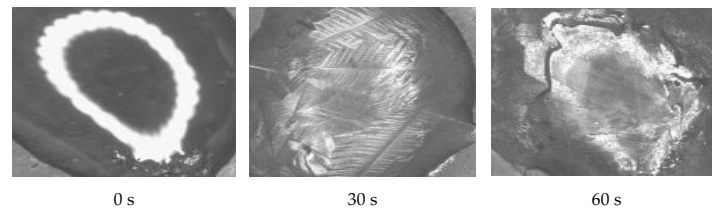
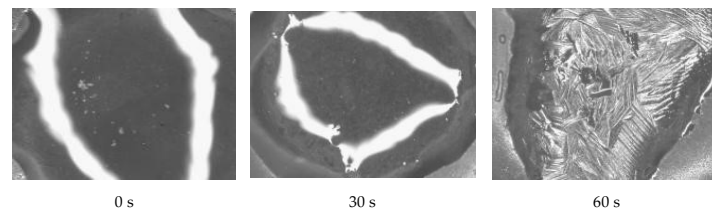


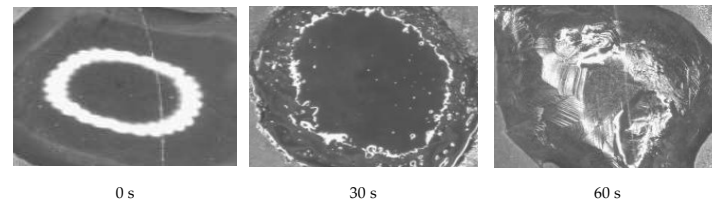
Figure 5. Growth morphology of hydrate at 2 °C (100 magnification).



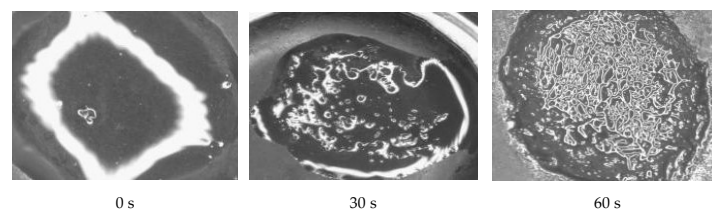
Growth morphology of hydrate at -1 °C (20% THF).



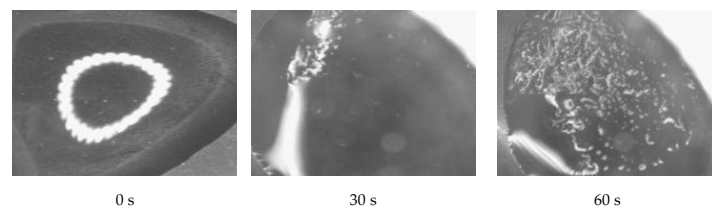
Growth morphology of hydrate at -1 °C (20% THF and integrated agent).



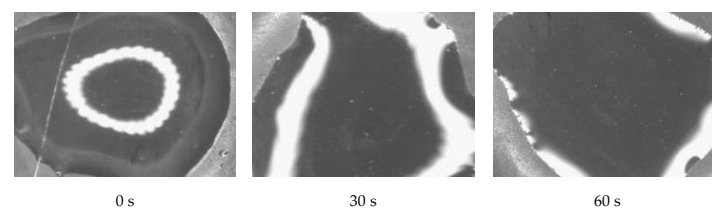
Growth morphology of hydrate at 0 °C (20% THF).



Growth morphology of hydrate at 0 °C (20% THF and integrated agent).



Growth morphology of hydrate at 1 °C (20% THF).



Growth morphology of hydrate at 1 °C (20% THF and integrated agent).

Figure 6. Microscopic view of hydrate formation of bulk agent at different temperatures.

3.11. Contact-Angle Experiment

As shown in Figure 7, compared to the cleaned-glass surface after treatment, the glass surface soaked with the integrated agent was significantly more hydrophilic and oil friendly. Through measurement, it was found that the integrated agent had better hydrophilicity, which is consistent with the anti-aggregation mechanism. On the one hand, the hydrophilic groups of the integrated agent were adsorbed on the surface of the hydrate, while the surfaces of adjacent hydrates were prevented from approaching each other due to the hydrophobic and hydrophilic groups' charge properties; On the other hand, the addition of an all-in-one agent disrupted the activity of the water molecules by hydrophilic groups, resulting in a decrease in the amount of hydrate formation. The anti-aggregation mechanism of the hydrates is shown in Figure 8.

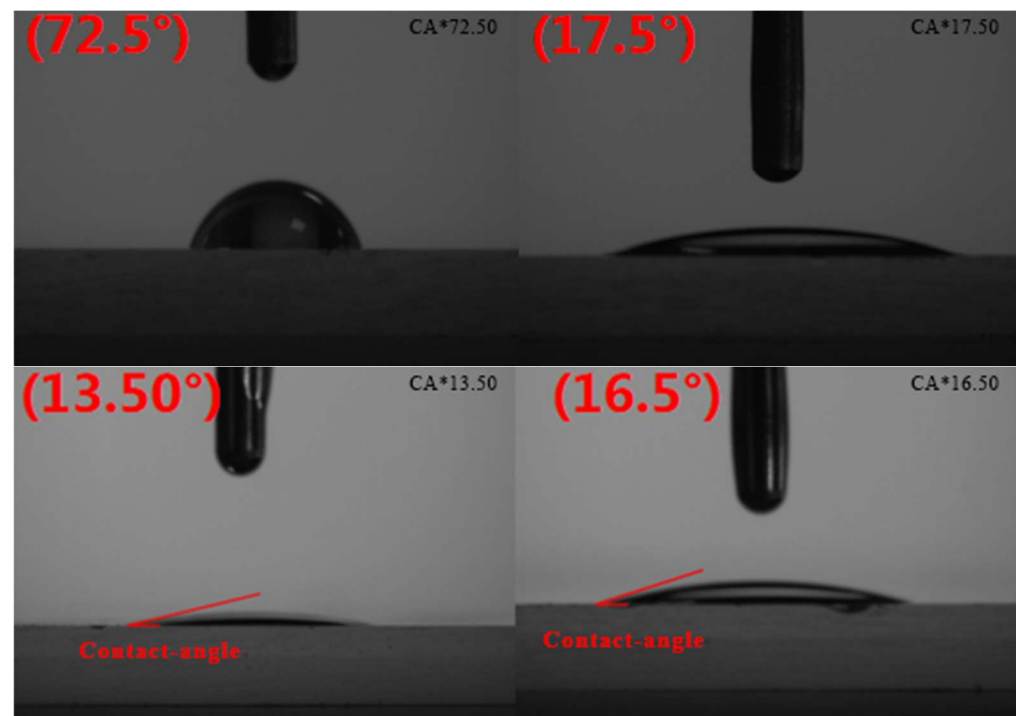


Figure 7. Contact-angle measurement of the one-piece agent (water at the top, oil at the bottom).

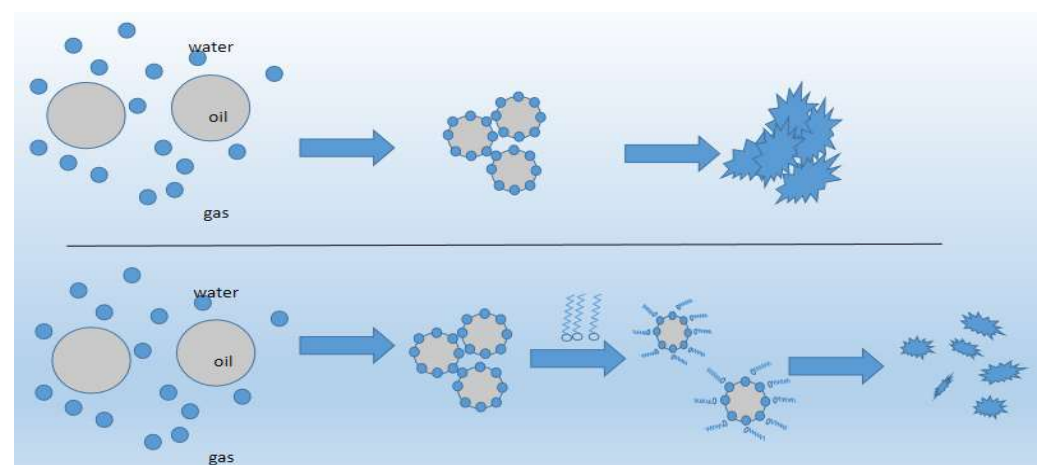


Figure 8. Anti-aggregation mechanism diagram.

3.12. Thermodynamic Analysis of Hydrates

As shown in Figure 9, with the operation of the cooling program, the solution gradually transformed from liquid to solid, and the formation of hydrates released heat, resulting in a change in calorific value. As a result, an upward heat release peak appeared in the image. At this time, the initial point of heat change was the phase transition point of the hydrates. As shown on the left of Figure 9, the phase transition point of 20% THF hydrate was 4.32 °C, indicating that THF hydrate begins to grow at this temperature. The right side of Figure 9 shows the phase transition point of the hydrate after the addition of an integrated agent. Compared with the 20% THF hydrate, the phase transition point decreased by 1.92 °C, significantly reducing the risk of hydrate formation. This is because the molecules of the integrated agent not only hinder the hydrogen bonding of water molecules to form a cage-like structure of hydrates, but also interfere with the activity of the water molecules, effectively reducing the aggregation of water and matter.

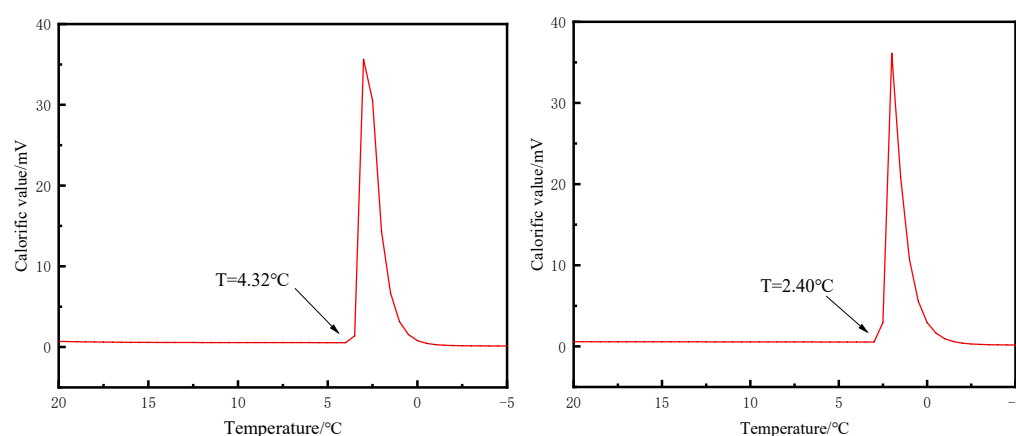


Figure 9. DSC curve of 20% THF solution with and without the integrated agent ((left) is without integrated agent; (right) is with integrated agent).

3.13. Emulsification Experiment and Microstructure Analysis after Emulsification

As shown in Figure 10, with the increase in the concentration of the integrated agent, the stability of the emulsion after uniform emulsification increased, and the amount of water released at the same time decreased. When standing at 45 °C for 1 min, the water evolution rates of different concentrations were 18, 12, 0, and 0%, respectively, indicating that the emulsion has good stability in a short period of time and can ensure good emulsification performance. After standing at 45 °C for 10 min, the water separation rate of the solution was 100, 74, 0 and 0%, respectively, which indicates that there is no difficult demulsification of lotion at 10 min, which is conducive to subsequent recovery. As shown in Figure 11, the amount and rate of water evolution at different concentrations increased with time and eventually stabilized. The emulsification performance of the integrated agent represents both the ability to foam and the ability to prevent hydrate aggregation. The better emulsification stability of the integrated agent is of great significance for the production of natural gas.

It can be seen from Figure 12 that at 0 min, the sizes of the lotions formed by mixing different concentrations of integrated agent and crude oil in a ratio of 1:1 were different. As the concentration of the integrated agent increased, the diameter of the emulsion became smaller, and the more small emulsions there were, the better the emulsifying ability and stability. In the figure, it can be seen that, as time went on, after emulsification with 1 and 1.5 times the emulsion, the emulsion continued to coalesce and its stability gradually deteriorated, providing the conditions for the demulsification of the emulsion. As the emulsion is an oil-in-water type, the integrated agent adsorbs at the oil–water interface, preventing the dispersed water droplets in the oil phase from coalescing in one place.

The oil-in-water type emulsion is more likely to improve the performance of the anti-aggregation agent.

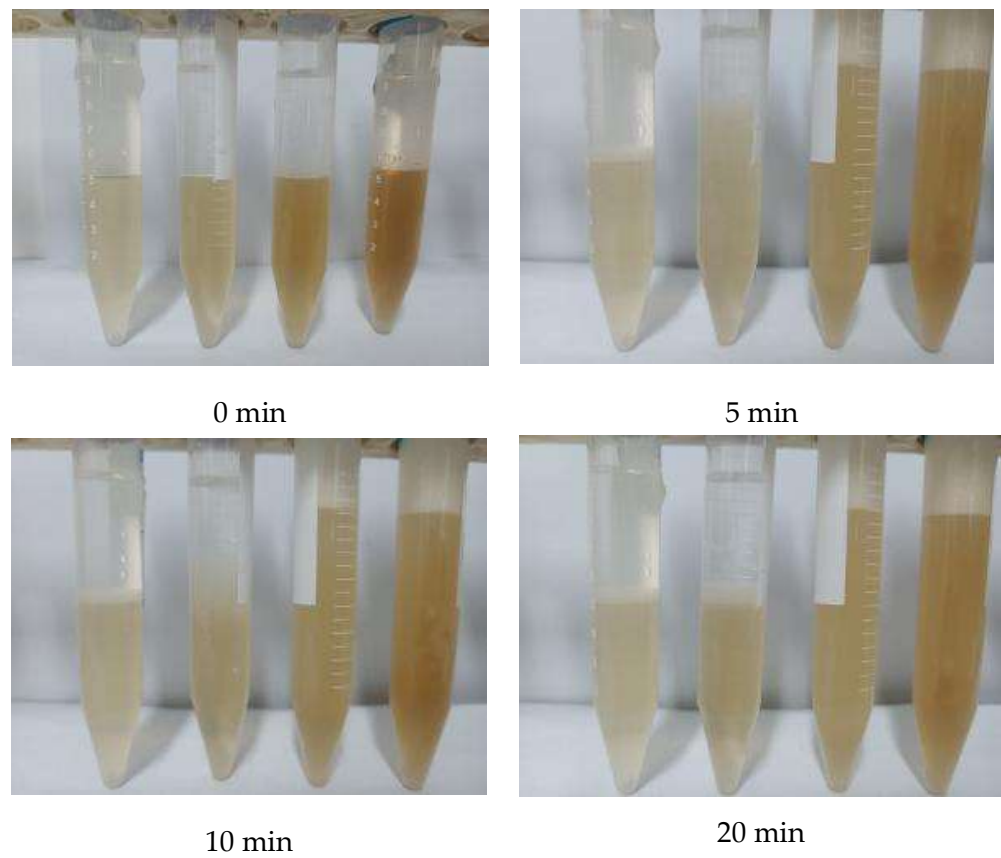


Figure 10. Emulsification experiments of different concentrations of the all-in-one agent (from left to right, 0.5, 1, 1.5, and double concentrations of the one-body solution).

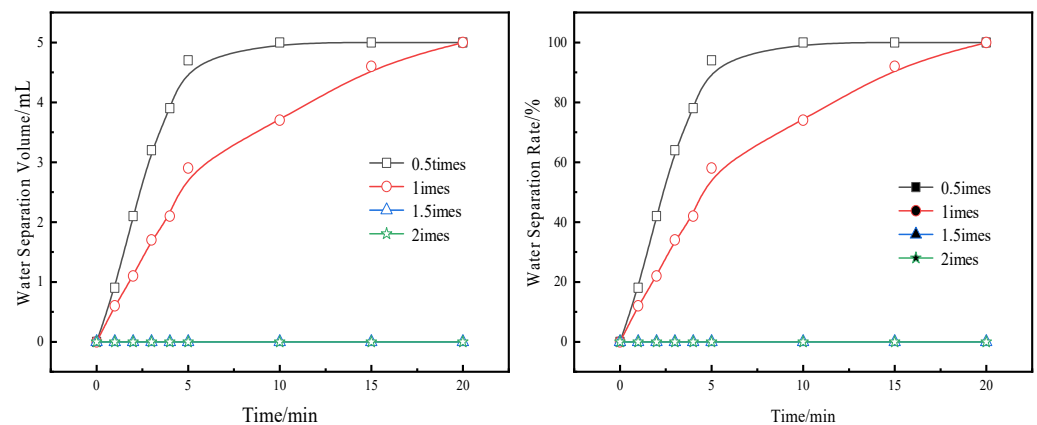


Figure 11. The water separation rate of the all-in-one emulsion at different times.

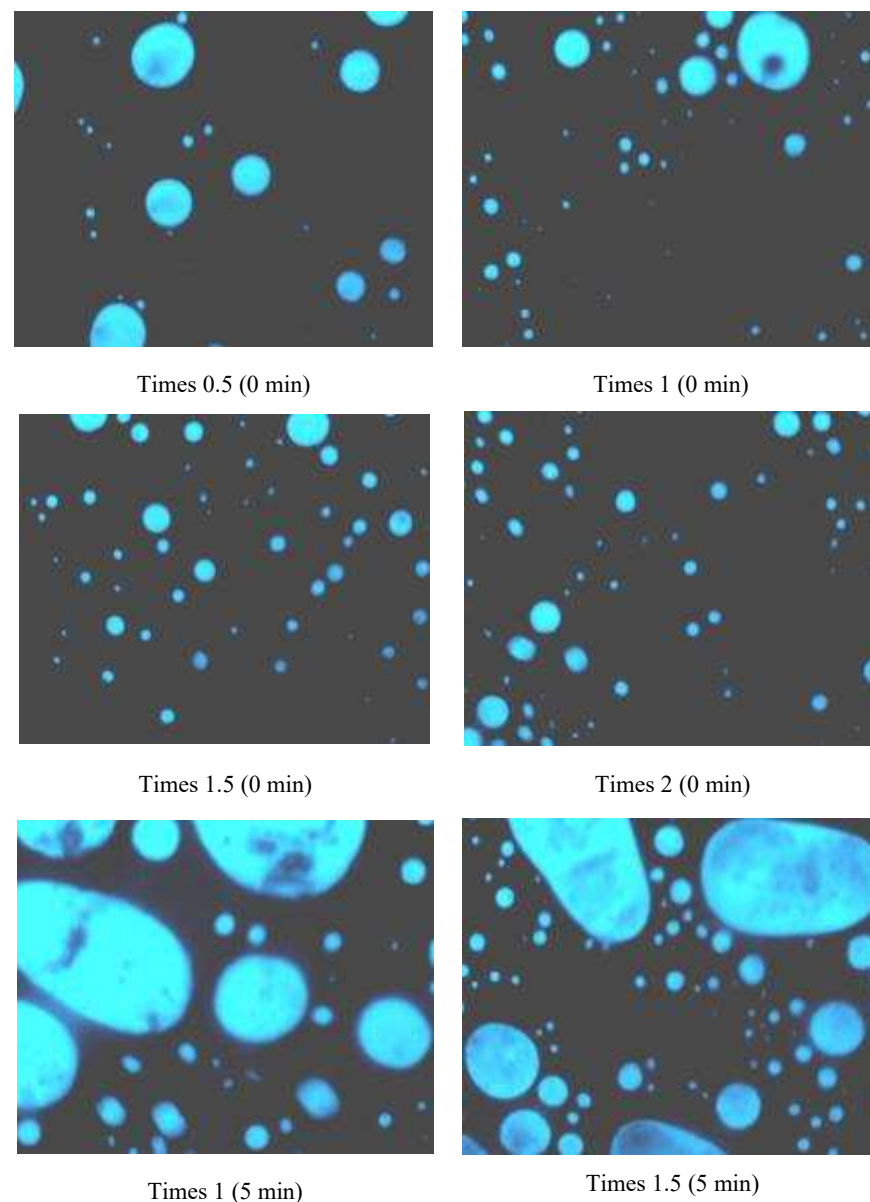


Figure 12. Microemulsion at different concentrations.

4. Conclusions

In this study, the final integrated formulation was determined: 0.1% sodium alpha-olefin sulfonate (AOST) + 0.3% dodecyl dimethyl betaine (BS-12) + 0.3% sodium ligno-sulfonate + 0.5% hydrazine hydrate. With this formulation, the performances of foaming, polymerization prevention and corrosion inhibition were improved. After adding this integrated agent, the growth rate of hydrates was slow and the maximum corrosion depth decreased to 5.24 μm . The good performance of this anti-aggregation agent is largely because of its oil-in-water type emulsion, preventing the dispersed water droplets in the oil phase from coalescing in one place. These excellent abilities to produce foam and inhibit corrosion indicate that they can be used in the oil and petrochemical industry for foam drainage and to inhibit corrosion, which have a certain practical uses.

Author Contributions: W.N.: data curation, investigation and writing—original draft; G.Y.: validation, conceptualization, supervision; J.D.: data curation, investigation, formal analysis; Y.P.: investigation, methodology, data curation; X.G.: project administration, funding acquisition; G.C.: writing—review and editing, validation, and supervision. All authors have read and agreed to the published version of the manuscript.

Funding: This work is funded by Scientific Research Program Funded by Shaanxi Provincial Education Department (Program No. 22JY052).

Data Availability Statement: The data that support the findings of this study are available from the corresponding author upon reasonable request.

Acknowledgments: The authors also thank the support of The Youth Innovation Team of Shaanxi University and the work of the Modern Analysis and Testing Center of Xi'an Shiyou University.

Conflicts of Interest: The authors declare no conflict of interest.

References

1. Zhang, T.; Wang, S.Z.; Dong, C.H. Experimental study on the emergency disposal agent for methanol leakage. *Adv. Mat. Res.* **2017**, *1142*, 306–313. [[CrossRef](#)]
2. Gu, X.F.; Gao, L.; Li, Y.F.; Dong, K.; Zhang, J.; Du, W.C.; Qu, C.T.; Chen, G. Performance and mechanism of span surfactants as clean flow improvers for crude oil. *Pet. Chem.* **2020**, *60*, 140–145. [[CrossRef](#)]
3. Behera, M.R.; Varade, S.R.; Ghosh, P.; Paul, P.; Negi, A.S. Foaming in micellar solutions: Effects of surfactant, salt, and oil concentrations. *Ind. Eng. Chem. Res.* **2014**, *53*, 18497–18507. [[CrossRef](#)]
4. Qu, C.; Wang, J.; Yin, H.; Lu, G.; Li, Z.; Feng, Y. Condensate oil-tolerant foams stabilized by an anionic–sulfobetaine surfactant mixture. *ACS Omega* **2019**, *4*, 1738–1747. [[CrossRef](#)]
5. Negm, N.A.; El Faragy, A.F.; Mohammed, D.E.; Mohamad, H.N. Environmentally friendly nonionic surfactants derived from tannic acid: Synthesis, characterization and surface activity. *J. Surfactants Det.* **2012**, *15*, 433–443. [[CrossRef](#)]
6. Lee, J.J.; Nikolov, A.; Wasan, D. Surfactant micelles containing solubilized oil decrease foam film thickness stability. *J Colloid Interface Sci.* **2014**, *415*, 18–25. [[CrossRef](#)] [[PubMed](#)]
7. Yoshimura, T.; Ichinokawa, T.; Kaji, M.; Esumi, K. Synthesis and surface-active properties of sulfobetaine-type zwitterionic gemini surfactants. *Colloids Surf. A* **2006**, *273*, 208–212. [[CrossRef](#)]
8. Li, Y.; Bai, Q.; Li, Q.; Huang, H.; Ni, W.; Wang, Q.; Xin, X.; Zhao, B.; Chen, G. Preparation of Multifunctional Surfactants Derived from Sodium Dodecylbenzene Sulfonate and Their Use in Oil-Field Chemistry. *Molecules* **2023**, *28*, 3640. [[CrossRef](#)] [[PubMed](#)]
9. Chen, G.; Cheng, C.; Zhang, J.; Sun, Y.; Hu, Q.; Qu, C.T.; Dong, S.B. Synergistic effect of surfactant and alkali on the treatment of oil sludge. *J. Petrol. Sci. Eng.* **2019**, *183*, 106420. [[CrossRef](#)]
10. Koczko, K.; Tselnik, O.; Falk, B. Silicon-based foamants for foam assisted lift of aqueous-hydrocarbon mixtures. In Proceedings of the SPE International Symposium on Oilfield Chemistry, The Woodlands, TX, USA, 11–13 April 2011; OnePetro: Richardson, TX, USA, 2011. [[CrossRef](#)]
11. Chen, G.; Lin, J.; Liu, Q.N.; Zhang, J.; Wu, Y.; Li, H.; Ma, Y.; Qu, C.T.; Song, W.Q. Corrosion inhibition and the structure-efficiency relationship study of two cationic surfactants. *Anti-Corros. Methods Mater.* **2019**, *66*, 388–393. [[CrossRef](#)]
12. Pavelyev, R.S.; Zaripova, Y.F.; Yarkovoi, V.V.; Vinogradova, S.S.; Razhabov, S.; Khayarov, K.R.; Nazarychev, S.A.; Stoporev, A.S.; Mendgaziev, R.I.; Semenov, A.P.; et al. Performance of Waterborne Polyurethanes in Inhibition of Gas Hydrate Formation and Corrosion: Influence of Hydrophobic Fragments. *Molecules* **2020**, *25*, 5664. [[CrossRef](#)]
13. Elhenawy, S.; Khraishah, M.; Almomani, F.; Al-Ghouti, M.A.; Hassan, M.K.; Al-Muhtaseb, A. Towards Gas Hydrate-Free Pipelines: A Comprehensive Review of Gas Hydrate Inhibition Techniques. *Energies* **2022**, *15*, 8551. [[CrossRef](#)]
14. Mandal, S.; Bej, S.; Banerjee, P. Insights into the uses of two azine decorated d10-MOFs for corrosion inhibition application on mild steel surface in saline medium: Experimental as well as theoretical investigation. *J. Mol. Liq.* **2023**, *381*, 109846. [[CrossRef](#)]
15. Raviprabha, K.; Bhat, R.S. Corrosion inhibition of mild steel in 0.5 M HCL by substituted 1,3,4-oxadiazole. *Egypt. J. Pet.* **2023**, *32*, 1–10. [[CrossRef](#)]
16. Pasha, T.; Mulaudzi, V.L.; Cele, M.L.; Mothapo, M.P.; Ratshisindi, F. Evaluation of corrosion inhibition effect of glycerol stearate on aluminium metal by electrochemical techniques. *Arab. J. Chem.* **2023**, *16*, 104798. [[CrossRef](#)]
17. Zhang, H.; Pang, X.; Gao, K. Localized CO₂ corrosion of carbon steel with different microstructures in brine solutions with an imidazoline-based inhibitor. *Appl. Surf. Sci.* **2018**, *442*, 446–460. [[CrossRef](#)]
18. Christogonus, A.O.; Arinze, C.M. Experimental and DFT evaluation of adsorption and inhibitive properties of Moringa oliefera extract on mild steel corrosion in acidic media. *Arab. J. Chem.* **2020**, *13*, 9270–9282. [[CrossRef](#)]
19. Bai, Y.; Zhang, J.; Dong, S.; Li, J.; Zhang, R.; Pu, C.; Chen, G. Effect of anion on the corrosion inhibition of cationic surfactants and a mechanism study. *Desalination Water Treat.* **2020**, *188*, 130–139. [[CrossRef](#)]
20. Enabulele, D.O.; Bamigboye, G.O.; Solomon, M.M.; Durodola, B. Exploration of the Corrosion Inhibition Potential of Cashew Nutshell on Thermo-Mechanically Treated Steel in Seawater. *Arab. J. Sci. Eng.* **2022**, *48*, 223–237. [[CrossRef](#)]
21. Hussain, H.H.; Husin, H. Review on Application of Quaternary Ammonium Salts for Gas Hydrate Inhibition. *Appl. Sci.* **2020**, *10*, 1011. [[CrossRef](#)]
22. Paz, P.; Netto, T.A. On the Rheological Properties of Thermodynamic Hydrate Inhibitors Used in Offshore Oil and Gas Production. *J. Mar. Sci. Eng.* **2020**, *8*, 878. [[CrossRef](#)]
23. Habib, S.; Nawaz, M.; Kahraman, R.; Ahmed, E.M.; Shakoore, R.A. Effect of the modified hybrid particle on the corrosion inhibition performance of polyolefin based coatings for carbon steel. *J. Sci. Adv. Mater. Devices* **2022**, *7*, 100466. [[CrossRef](#)]

24. Xu, X.; Wei, H.Y.; Liu, M.G.; Zhou, L.S.; Shen, G.Z.; Li, Q.; Hussain, G.; Yang, F.; Fathi, R.; Chen, H.G.; et al. Nitrogen-doped carbon quantum dots for effective corrosion inhibition of Q235 steel in concentrated sulphuric acid solution. *Mater. Today Commun.* **2021**, *29*, 102872. [[CrossRef](#)]
25. Ulhaq, M.I.; Saleem, Q.; Ajwad, H.; Aleisa, R.M.; Alanazi, N.M.; Leoni, M.; Zahrani, I.; Makogon, T. Corrosion inhibition of carbon steel in a sour (H₂S) environment by an acryloyl-based polymer. *ACS Omega* **2023**, *8*, 18047–18057. [[CrossRef](#)]
26. Obot, I.B.; Obi-Egbedi, N.O. Adsorption properties and inhibition of mild steel corrosion in sulphuric acid solution by ketoconazole: Experimental and theoretical investigation. *Corros. Sci.* **2009**, *52*, 198–204. [[CrossRef](#)]
27. Jiang, L.L.; Xu, N.; Liu, Q.B.; Cheng, Z.C.; Liu, Y.; Zhao, J.F. Review of Morphology Studies on Gas Hydrate Formation for Hydrate-Based Technology. *Cryst. Growth Des.* **2020**, *20*, 8148–8161. [[CrossRef](#)]
28. Zandi, M.S.; Hasanzadeh, M. The self-healing evaluation of microcapsule-based epoxy coatings applied on AA6061 Al alloy in 3.5% NaCl solution. *Anti-Corros. Methods Mater.* **2017**, *64*, 225–232. [[CrossRef](#)]
29. Sliem, M.H.; El Basiony, N.M.; Zaki, E.G.; Sharaf, M.A.; Abdullah, A.M. Corrosion Inhibition of Mild Steel in Sulfuric Acid by a Newly Synthesized Schiff Base: An Electrochemical, DFT, and Monte Carlo Simulation Study. *Electroanalysis* **2020**, *32*, 3145–3158. [[CrossRef](#)]
30. El-Hajjaji, F.; Ech-Chihbi, E.; Rezki, N.; Benhiba, F.; Taleb, M.; Chauhan, D.S.; Quraishi, M. Electrochemical and theoretical insights on the adsorption and corrosion inhibition of novel pyridinium-derived ionic liquids for mild steel in 1 M HCl. *J. Mol. Liq.* **2020**, *314*, 113737. [[CrossRef](#)]
31. Navidfar, A.; Bulut, O.; Baytak, T.; Iskender, H.; Trabzon, L. Boosted viscoelastic and dynamic mechanical behavior of binary nanocarbon based polyurethane hybrid nanocomposite foams. *J. Compos. Mater.* **2022**, *56*, 2907–2920. [[CrossRef](#)]
32. Alaboalirat, M.; Qi, L.; Arrington, K.J.; Qian, S.; Keum, J.K.; Mei, H.; Littrell, K.C.; Sumpter, B.G.; Carrillo, J.M.; Verduzco, R.; et al. Amphiphilic Bottlebrush Block Copolymers: Analysis of Aqueous Self-Assembly by Small-Angle Neutron Scattering and Surface Tension Measurements. *Macromolecules* **2019**, *52*, 465–476. [[CrossRef](#)]
33. Dong, S.B.; Liu, C.W.; Han, W.W.; Li, M.Z.; Zhang, J.; Chen, G. The Effect of the Hydrate Antiagglomerant on Hydrate Crystallization at the Oil-Water Interface. *ACS Omega* **2020**, *5*, 3315–3321. [[CrossRef](#)]

Disclaimer/Publisher's Note: The statements, opinions and data contained in all publications are solely those of the individual author(s) and contributor(s) and not of MDPI and/or the editor(s). MDPI and/or the editor(s) disclaim responsibility for any injury to people or property resulting from any ideas, methods, instructions or products referred to in the content.